Solidification and fcc to metastable hcp phase transition in krypton under variable compression rates

Jing-Yin Chen, Choong-Shik Yoo, William J. Evans, Hanns-Peter Liermann, Hyunchae Cynn, Minseob Kim, and Zsolt Jenei

Phys. Rev. B **90**, 144104 — Published 15 October 2014

DOI: 10.1103/PhysRevB.90.144104

Solidification and fcc- to metastable hcp- phase transition in krypton under variable compression rates

Jing-Yin Chen[1], Choong-Shik Yoo[2], William J. Evans[1], Hanns-Peter Liermann[3], Hyunchae Cynn[1], Minseob Kim[2], and Zsolt Jenei[1]

[1]CMMD, Physical & Life Science Directorate, Lawrence Livermore National Laboratory, Livermore, California 94551, USA

[2]Department of Chemistry, Institute for Shock Physics, Washington State University, Pullman, Washington 99164, USA

[3]Photon Sciences, Deutsches-Elektronen Synchrotron DESY, D-22603 Hamburg, Germany

ABSTRACT

We present time-resolved synchrotron x-ray diffraction measurements to study kinetics associated with the liquid-solid and solid-solid high-pressure phase transitions in Kr under dynamic loading in a *dynamic*-diamond anvil cell (*d*-DAC). The results show a strong compression-rate dependence of the solidification/melting process in liquid Kr. The analysis of the compression-rate dependent melting/solidification, using an Avrami equation with the parameter n=1 indicates a spontaneous nucleation and one-dimensional growth mechanism. In contrast, the *fcc* to metastable *hcp* transition in solid Kr occurs rapidly at ~0.8 GPa near the melting line, which has negligible compression rate dependence within the range of compression rates studied (0.004-13 GPa/s).

INTRODUCTION

Understanding the dynamic response of solid under extreme conditions of pressure, temperature and strain rate is a fundamental scientific quest and a basic research need in materials science. Specifically, obtaining an atomistic description of structural and chemical changes of solid under rapid heating and/or compression over a large temporal, spatial and energy range is challenging but critical to understanding material stability or metastable structure, chemical mechanism, transition dynamic, and mechanical deformation. In this regard, developing time-resolved x-ray diffraction applied to solids under dynamic conditions is timely and synergistic to many proposed activities centered at third- and fourth-generation light sources.

Critical to high-pressure kinetic studies is the ability to precisely control pressure and compression rates over a wide range of governing time scales. Solid-state transformations under static high pressures are typically diffusion-limited, occurring in an intermediate time scale of μs to ms and between those of conventional static (<1 GPa/s) and shock wave (>10^7 GPa/s) compressions. This is the time scale or compression rate that can be obtained, in a controlled way, using dynamic-diamond anvil cells (*d*-DAC) [1-5]. Hence, in this study we combined *d*-DAC with time-resolved synchrotron x-ray diffraction to probe structural evolutions and transition dynamics associated with melting and phase transitions of krypton under dynamic pressure loadings.

Noble gases liquids, with the exception of helium, crystalize into a face-centered cubic (*fcc*) structure at low temperatures or at elevated pressures. Theoretical calculations [6,7], however, predict a diminishingly small energy difference as a function of pressure between *fcc* and hexagonal close packed (*hcp*) structures in noble gas solids. In fact, a series of sluggish transitions have been found in *fcc*-Xe under pressures, first to an intermediate close-packed

phase at ~ 14 GPa, then, to *hcp* above 75 GPa [8]. The sluggish nature of the transition in solid Xe often resulted in large stacking disorders in the *fcc* lattice and both *fcc* and *hcp* phases being observed over a wide pressure range between 3 and 70 GPa after high temperature annealing by laser heating [9,10]. Xenon metallizes above 130 GPa [8,11-12], presumably in this high-pressure *hcp* phase. A similar *fcc* to *hcp* transition was also observed in laser-heated Kr at the pressure range of 3 to 50 GPa [13].

Electronic structure calculations [7] have suggested that the hybridization between the *s/p*- and *d*- bands favors the *hcp* structure of Xe at high pressures before it metallizes at ~130-150 GPa [11-12]. However, because of small energy difference between the *fcc* and *hcp* structures it is difficult to depict the onset of the transition. The *fcc*-to-*hcp* transition in Kr, on the other hand, has been predicted to occur well above 130 GPa [14] – substantially higher than the pressure range (3-50 GPa) previously observed [13]. This difference is likely due to the presence of shear in the sample that can introduce the stacking disorder well below the transition pressure.

The *fcc* structure has an ABC packing order along the body diagonal, while the *hcp* structure has an AB packing order along the c-axis. Due to numerous slip systems in close-packed structures, imposition of shear or differential stresses can lead to an *fcc*-to-*hcp* transition, which is often observed in closed-packed metals [15-18]. However, it is also important to note that the stacking disorder is not the only mechanism causing the *fcc*-to-*hcp* transition. The *hcp* structure, for example, has previously been observed upon the rapid solidification of laser-heated Kr at substantially lower pressures (below 50 GPa) [8-10]. As such, it appears to signify other mechanisms governing the transition including lattice defects and disorders.

In order to understand the *fcc*-to-*hcp* transition mechanism, we have investigated Kr under dynamic loadings in *d*-DAC and measured the structural changes associated with the

pressure-induced melting/solidification and *fcc*-to-*hcp* transitions in Kr over a wide range of compression rates. The present experiments have been performed at relatively low pressure at room temperature – in the range far from the predicted fcc-hcp transition but near the melting where the formation of defects and stacking disorders can play significant roles depending on the compression rates.

EXPERIMENTS

High purity krypton gas (>99.995%, Alfa Aesar) was used without further purification. Kr was loaded cryogenically into a small hole (0.08-0.13 mm in diameter) of a pre-indented stainless steel gasket mounted between two opposed diamond anvils with 0.3 mm culets, together with a few small ruby spheres and copper powder for pressure estimation. Based on the micro-photographic image and x-ray diffraction pattern, the loaded Kr shows no apparent trace of impurities.

Time-resolved x-ray diffraction experiments were carried out using monochromatic synchrotron x-rays at 25.7 keV (0.48262 Å) at the Extreme Conditions Beamline (ECB) P02.2 at PETRA III, Deutsches Elektronen Synchrotron (DESY). The incident x-ray beam was focused to a spot size of full width half maximum, ~ 2 (H) x 7 (V) μm^2 using a compound refractive lens system (CRL) and the 2-dimensional diffraction pattern was collected using a Pilatus 1M area detector. Electronic instrumentation was used for synchronization, triggering and monitoring the timing between the x-ray detector and *d*-DAC; including a piezo-actuator power amplifier, a function generator, a delay generator, and a digital oscilloscope.

For these studies, we utilized a *d*-DAC, which adapts three piezo-electric actuators (Piezo Jenna) into a conventional DAC [19]. The loading profiles of the piezo-electric actuators, including peak pressure (P), pressure modulation (ΔP), compression rate (ΔP/Δt), and load frequencies (*f*), are precisely controlled by the applied waveform of the electric drive signal, as shown in Fig. 1. The diagram shows the timing of a representative experiment, recorded by an oscilloscope, and includes the pressure modulation (black) and the feedback signal of the Pilatus detector (gray), in comparison to the measured pressure (solid circles) and sample lattice parameters (open diamonds). The arrows indicate when the trigger pulses were sent to the function generator and the detector. The sample pressure was estimated from the measured Cu (111) peak position using the equation of state (EOS) previously reported [20]. This is because the (111) reflection is the most dominant feature observed in all our diffraction data. We used three types of waveforms (sine, square and trapezoid waves) to generate the pressure modulation across the liquid-solid transition. Note that there is a small time delay between the observed Cu and Kr pressure (or lattice) shifts. This delay originates from the difference in compressibility between Cu and Kr samples. The compression (or decompression) rate of the experiment is estimated by the rising (or falling) slope of the determined pressure versus time.

Series of x-ray diffraction images were collected with varying exposure times at the frequency range of 2 (500 ms x-ray exposure) to 33 (30 ms) Hz. Three selected diffraction images of one diffraction experiment are shown in Fig. 2a. We used the Fit2D program [21] to process the diffraction images and convert them to intensity vs 2θ plots (as shown in Fig. 2b) or a 2D contour plot to examine the lattice response to the pressure variation (in Fig. 2c). For comparison, the solid bars at the top of Fig. 2c represent the calculated peak positions for Cu and *fcc*- and *hcp*-Kr at 1.1 GPa using CrystalMaker®. Figure 2c illustrates a series of dynamic

loadings of Kr, consisting of five consecutive, one-second-long truncated sine wave pressure modulations. Note that at the beginning of the experiment, Kr is in the liquid state, solidifies into the *fcc* phase and then transforms into an *hcp* structure during compression. Upon decompression, both the *fcc* and *hcp* phases melt, but only partially; a remnant of *fcc* phase persists. During the five consecutive pressure modulations, not all of diffraction peaks appear in each cycle. Some diffraction peaks appear and develop after a brief delay.

We analyzed the measured angle-resolved diffraction patterns in Fig. 2b using Jade® (MDI, Jade 9) to index the diffraction peaks of Cu and the high-pressure polymorphs of Kr. Then, we analyzed the spectral shape of each indexed peak using Matlab® to locate the peak position, the intensity at the peak center and the integrated intensity of the peak, for further kinetic analysis. The indexed peak positions give the lattice parameters for Cu, *fcc*-Kr and *hcp*-Kr.

RESULTS

Krypton is initially in liquid state, as indicated by the first broad diffuse diffraction ring at around $2\theta = 9^{o}$ illustrated in Fig. 3a and the very weak second broad diffraction ring located at $2\theta = \sim 15.5^{o}$. The solidification process is studied by tracking the spectral changes on this broad liquid diffraction line with pressure. The intensity of the broad liquid peak gets weaker and the peak position shifts toward a slightly higher angle, as pressure increases. The change in the diffraction intensity, or the peak area calculated by integrating the area beneath the peak, is notable with the pressure change, as illustrated in Fig. 3b. The integrated peak area (solid circles) and the measured pressure (open diamonds) are represented as a function of time of the pressure loading in Fig. 3b. Note that liquid and solid Kr coexist over a small pressure range after the

crystallization starts. This is due to the fact that the pressure increase stagnates at the transition pressure and the driving peak pressure remains slightly lower than (or near) the equilibrium solidification pressure, ~ 0.9 GPa.

The analysis shows that the peak area in Fig. 3b decreases (or increases) exponentially with time during the compression (or decompression) at the onset of solidification (or melting) of the Kr. This peak area change can be described in terms of a simple exponential decay/growth equation as represented in the red curves; $Y=1-a*\exp(-t^n/\tau)$ where τ is the decay/growth time constant with a = -0.676±0.04, τ = 0.599±0.04 s and n=1. This fact, a simple exponential equation represents the growth (nucleation) equation, indicates there is little contribution from pressure during solidification or melting once the dynamic pressure loading is enough to initiate the process. According to the Avrami equation [22], a simple exponential fit (n=1) of the liquid-solid and solid-liquid transitions implies a homogeneous nucleation process, in which all nucleation occurs spontaneously in a supercooled (or supercompressed in the present case) state and there is one-dimensional growth of solid/liquid (a rod-shaped product). This result probably reflects the hydrodynamic nature of dynamic pressure loading (or unloading) in the *d*-DAC, which drives the Kr sample into a supercompressed (or undercompressed) state near the diamond-Kr interfaces while the mean pressure still remains unchanged. Based on the data in Fig 3, we estimate that the Kr sample at the interfacial region is supercompressed by ~0.3 GPa to 0.8 GPa, sufficient to initiate the solidification process at the mean pressure of 0.5 GPa.

In figure 4, we present the solidification or melting time constant defined as τ from the exponential fit as a function of compression (solid circles) or decompression (open circles) rates. As expected, the solidification (or melting) time constants increase as the compression (or decompression) rate decreases (Fig. 4). Note that they follow a linear relationship in the

logarithmic plot (Fig. 4 inset) with a slope of 0.72 (±0.06) GPa^{-1} for the solidification and 0.63 (±0.2) GPa^{-1} for the melting. This indicates a similar mechanism governing both the crystallization and melting. A similar linear relationship between the compression rate and the growth rate has often been observed in other solid-solid transformations [22-23]. The slope is related to the activation energy; yet, the time resolution of the experiments in the present study is not sufficient to resolve the transition pressure to extract activation energy, based on the transition state model [24].

Figure 5 shows contour plots of 2θ-time of diffraction patterns obtained under three different dynamic loadings with the compression rates of (a) ~8 GPa/s (50 ms exposure), (b) 1.9(±0.1) GPa/s (200 ms exposure) and (c) 0.005(±0.001) GPa/s (500 ms exposure). The calculated diffraction peak positions are also marked as vertical bars at the top: Cu (in black bars), *fcc*-Kr (in blue) and *hcp*-Kr (in red) at 1.1 GPa, as well as the measured pressure at the right of the figure. Note that there is a time delay during decompression between the initial pressure decreases as estimated by Cu EOS and the start of the shift of the diffraction peaks of Kr. This discrepancy is due to the difference in compressibility of Cu and Kr.

Upon the fast compression at 8 GPa/s in Fig. 5a, the *fcc* phase of Kr appears nearly instantaneously as the pressure increases, while a *hcp* phase appears after a delay of ~1 second. The presence of the *hcp* is apparent from the appearance of at least three diffraction peaks (100), (102) and (200) with 2θ values of 8.46, 12.2, and 16.9 respectively. Note that the (102) peak appears as a doublet, which likely represents stacking disorder in this metastable *hcp*-phase. In addition to the existence of metastable *hcp*, there are two un-identified diffraction peaks, appearing 0.2 second after the pressure increases at $2\theta \sim 14.7^{o}$. These two weak diffraction peaks diminished with time and are most likely related to the growth of the *hcp* diffraction peaks.

Since no other peaks are possibly related to *hcp* phase and the intensity changes of these two peaks at 14.7 degree correspond to the later development of a doublet of metastable *hcp* (102) peak, all of these peaks may indicate a presence of a stacking-disordered intermediate phase as a precursor to the *hcp* phase. It is possible to observe more disordered peaks or no peaks (indicating amorphous or plastic solid) when the compression rates are increased further. Additional high compression rate experiments with better time resolution are needed to clarify the plausibility of this mechanism. Solid Kr starts to melt as soon as the pressure decreases. As expected, the *hcp* disappears first, then the *fcc* about 1 second later. During the largest compression rate experiment of this study, the *hcp* diffraction peaks are all very weak, implying that faster compression/decompression suppresses the formation of *hcp* phase. In addition, the nucleation time of *fcc* phase is much faster than that of *hcp* phase at the higher compression rates.

At the intermediate compression rate of 1.9 GPa/s depicted in Fig. 5b, the *fcc* phase appears first during the compression period (or above 0.6 GPa) as is evident from several sharp diffraction peaks including (111) at 8.9 degree and (222) at 17.7 degree; then, the *hcp* phase starts to appear as the pressure reaches its peak pressure, as is evident from the (100), (101), (102), and (103) diffraction lines at ~8.4, 9.6, 12.3, and 15.9 degrees respectively. Upon decompression, the *hcp* phase disappears as soon as liquid Kr starts to appear, whereas the *fcc*-phase remains and coexists with liquid for at least 1 second. This reflects the metastable nature of *hcp* phase, which converts immediately back to the *fcc* phase or the melt as the stacking disorder immediately dissipates upon melting.

At a compression rate of 0.005 GPa/s in Fig. 5c, for example, there exists a large time delay between the sample response and the pressure modulation; ~9.7 s based on liquid Kr and ~

16.2 s based on Cu. This delay accounts for the late decrease of the area of the liquid ~20 s after the pressure increase (P ~ 0.6 GPa). Surprisingly, the *hcp*-Kr appears at ~ 29 s after the pressure change and dominates the solid phase. At ~ 33 s, the (111) peak of the *fcc*-Kr appears, which could also be interpreted as the (002) of the *hcp*-Kr. Furthermore, the remaining diffraction peaks associated with *fcc*-Kr are very weak, including (200), (220) and (311) at 10.3, 14.6, and 17.1 degree respectively. The fact that the *hcp*-Kr dominates at the slower dynamic loading implies that the kinetic energy favors the formation of *hcp*-Kr. A plausible explanation for the formation of the *hcp*-Kr phase when the compression rates are smaller than 0.005 GPa/s, is that the formation of defects and stacking faults are much easier when the pressure compression rates are too low to form the equilibrium *fcc* phase. At slow compression rates the transition to fcc is somewhat limited by a relatively high activation barrier with respect to the driving force and, instead, produces defects and stacking faults in the structure which require smaller formation energies.

Upon decompression, solid Kr expands first and then melts. During the melting process, the *hcp*-Kr disappears first, and then the *fcc* melts at all compression rates. Interestingly, at this slow dynamic loading, the amount of the *fcc*-Kr seems to increase first (~ 10% for (111) peak and 5% for (311)) before it converts to liquid. This may be due to the conversion of the *hcp*-Kr into the *fcc*-Kr (not to the melt).

Figure 6 shows the lattice parameter changes of (A) *fcc*- and (B) *hcp*-Kr upon the pressure modulations at the compression rate of 0.02 (±0.009) GPa/s, including both the lattice parameters from individual (hkl) planes (open symbols) and the average values (solid symbols). The compression rate, $\Delta P/\Delta t$, are estimated from the slope of pressure change from the measured Cu (111) diffraction line using the previously reported equation of state [20]. The $\Delta a/\Delta t$ of the

fcc phase, on the other hand, is obtained from the linear slopes of the lattice changes (red lines) during compression and decompression. The t_i^{fcc} (or t_i^{hcp}) denote the time when the first *fcc* (or *hcp*) diffraction peak appears, whereas the t_i^P (or t^P_{max}) denote the time when the pressure starts to increase (or reaches its maximum value). A delay between the sample responses and the modulation is observed, partially due to the delay of mechanical engagement of the piezo transducers and partially from the different sensitivities of Cu and Kr as described below. The large error bars on the calculated pressure compared to those of the calculated lattice parameters of Kr reflect the substantially greater compressibility of Kr phases in contrast to Cu. However, a systematic analysis allows meaningful comparisons among different dynamic loadings.

DISCUSSION

The volumes of *fcc* and *hcp*-Kr as a function of time/t_m (t_m is the duration for one modulation) are presented in Figure 7a. During dynamic loading, a ~2% volume compression (or decompression) is achieved. Clearly, the volumes of the *fcc* phase measured at different compression rates are in an excellent agreement with each other. The volume of the *hcp* phase deviates slightly from that of the *fcc*, when it initially forms, but it becomes the same during the decompression.

Note that there is a subtle difference in the measured volumes of the *hcp* phase at different compression rates; for example, those at 0.02 GPa/s compression rate are slightly larger than those at 0.07 and 1.9 GPa/s rates. The former agree well with the specific volumes of the *fcc* phase. This is interesting, because the metastable *hcp* phase becomes denser (by about 2%) than the stable *fcc* phase over the pressure range between 0.5 and 2 GPa, especially at the faster rate of compression. Nevertheless, it is consistent with a previous result [13], indicating that *hcp*-Kr, formed after laser-heating at high pressures of 20 GPa, is about 1.4% denser than the *fcc* phase.

Although the volume difference between the *hcp* and *fcc* phases is well within the error bar, this observation may be related to the fact that the amount of *hcp*-Kr dominates at slower dynamic loadings, discussed above. The c/a ratios of the *hcp*-Kr measured at different dynamic loadings (in Fig. 7a inset) show a relatively large range of 1.60 to 1.68 – reflecting a kind of stacking disorder in the *hcp* phase.

In figure 7b, we summarize the average volume compression curves of the *fcc* (solid circles) and *hcp* (open circles) phases in comparison with those previously measured in static (solid line) and laser-heating (solid and open diamonds) experiments [10,13], in the pressure range of 0.5-2 GPa. The volume data of Kr are the average value of all volume data at the same measured pressure for all measurements. The scattering experimental data in the range of 0.5 and 1.1 GPa imply that the hysteresis during the pressure cycling are observed for both *fcc*-Kr and *hcp*-Kr phases, which is demonstrated by the selected sets of measurements shown in the inset of Fig.7b. The hysteresis loop of the *fcc* phase is slightly larger than that of the *hcp* phase. At higher pressure (>1.1 GPa), the hysteresis is below the sensitivity of our detection for both phases. The static compression curve is produced using the third-order Birch-Murnaghan (B-M) EOS with the previously reported parameters of the isothermal bulk modulus (K_T =2.7 GPa), its first derivative with respect to pressure (K'=5.4) and the volume at ambient condition (V_0= 29.7 cm^3/mol) [13]. Again, the measured volumes of the *hcp* phase are very similar to those of the *fcc*, consistent with the coexistence of *hcp* and *fcc*. It also shows a subtle yet notable slope change in the pressure-volume curve at ~0.9 GPa – the previously reported solidification pressure [13]. Note that the extrapolation of the present compression curve agrees well with the previously observed volumes of the *fcc* (solid diamonds) and *hcp* (open diamond) phases under temperature

modulation at ~2.2 GPa [10]. Nevertheless, the dynamic EOS agrees well with the static EOS within the pressure difference by 0.3 GPa, as shown by the blue curve.

The measured strain rate ($\Delta a/a_o/\Delta t$) decreases linearly from +0.4/s to -0.4/s as the compression rates increases from -9 to 12 GPa/s, as shown in Fig. 8. As such, the present result demonstrates the elastic response of the *fcc* lattice under dynamic loading. The slope of the *fcc* lattice change rate, $\Delta a/\Delta t$ is -0.24(±0.01) Å/GPa. In fact, the measured linear compressibility, ~ 0.041(±0.002) GPa^{-1} is calculated by dividing a_0= 5.8213 Å from V_0 of B-M EOS [13]. Based on the reasonable assumption that *fcc* is isotropic, the isothermal compressibility, ~ 0.123 (±0.006) GPa^{-1} in this study is quite similar to the isothermal compressibility of *fcc*-Kr, 0.167 GPa^{-1}, derived from the adiabatic bulk modulus (Ks=6 GPa at 1 GPa) of Kr from energy-dispersive x-ray diffraction and Brillouin scattering [25]. Hence, based on this observation we conclude that the formation of the *hcp* phase is indeed induced by a simple stacking disorder of the *fcc* phase - not by the plastic deformation or twinning. A higher compression rate and/or higher pressure may be required to induce the plastic deformation of the *fcc* phase.

The induction times for the nucleation of the *fcc* and *hcp* phases can be estimated statistically as illustrated in Fig. 9. According to the Gaussian probability density function and the Gaussian fits shown in red, approximately 68% of the *fcc* phase nucleates and appears within -0.12 – 0.18 s from the instance of the pressure increase. In addition, approximately 68% of *hcp*-Kr appears in the time frame of -0.28 – 0.57 s after the pressure reach the peak value. The times of t_i^{fcc}, t_i^P, t_i^{hcp} and t^P_{max} are defined in Fig. 6. The number of measurements used for the *fcc* and *hcp* phases are, respectively, 51 and 40. The threshold transition pressure of the *hcp* phase is found to be ~ 0.8 GPa at the compression rates ranging from 0.004 to 13 GPa/s, as shown in the inset. Even though the time resolutions of the current studies are slow, the induction times of

this study provide valuable information for the future studies. In this study, the induction times of *fcc* and *hcp* phases have no compression rate dependence or are not quantifiable because of inadequate time resolution of our measurements. This result agrees very well with the observation of spontaneous nucleation observed in liquid Kr.

CONCLUSIONS

The solidification of Kr occurs through spontaneous nucleation of an *fcc* lattice, following a simple exponential decay of liquid Kr and the critical nucleation time of -0.12 – 0.18 s. Based on the Gaussian probability density analysis, the nucleation time of solid Kr is found to be independent of the compression rate over 0.004-13 GPa/s. The *fcc* lattice behaves elastically at all pressures and compression rates studied, which transforms into the metastable *hcp* phase at ~0.8 GPa. We found that the formation of *hcp*-Kr is most pronounced at the slowest compression rates (<0.005 GPa/s), suggesting a defect-assisted transition mechanism. As such, the slow compression rate produces a larger amount of defects in the *fcc* lattice, which can lower the transition barrier to the *hcp* phase under dynamic compressions. Consequently, the formation of the metastable *hcp* at low pressure under dynamic loading confirms the predicted small volume difference between *fcc* and *hcp* phases. The isothermal compressibility, ~ 0.123 (±0.006) GPa^{-1} measured in this study agrees reasonably well with that, 0.167 GPa^{-1} previously obtained from the energy-dispersive x-ray diffraction and Brillouin scattering [25]. The measured linear strain rate of the *fcc* phase supports the suggestion that the *fcc*-to-*hcp* transition arises from stacking disorder in the *fcc* phase - not by the plastic deformation or twinning.

Acknowledgments

This work at LLNL was performed under the auspices of the U.S. Department of Energy under contract W-7405-Eng-48 and DE-AC52-07NA27344 and supported by the Laboratory Directed Research and Development Program under project tracking code 11-ERD-046. The work at WSU was performed in support of NSF-DMR (Grant No. 1203834) and DTRA (HDTRA1-12-01-0020). We appreciate Ken Visbeck at LLNL for his assistance in sample preparations. The X-ray studies were performed at the light source PETRA III at DESY, a member of the Helmholtz Association (HGF).

Figure Captions

Fig. 1 One representative applied waveforms (black line) into piezo-actuators and the detector response (gray line) on the left vertical axis and the experimental pressures estimated from Cu (solid circles) and the lattice parameter of Kr-*fcc* (open diamonds) on the right vertical axes.

Fig. 2 (a) Three representative diffraction images during the modulations. The number stated in the image is the scan number of the modulation. (b) The integrated diffraction patterns from the selected images. (c) A 2θ-scan_number plot of a series of time-resolved diffraction measurements with 50 ms exposure time, consisting of five consecutive, one-second-long truncated sine wave pressure modulations and the calculated diffraction patterns of Cu (black), Kr-*fcc* (blue) and Kr-*hcp* (red) at 1.1 GPa.

Fig. 3 (A) A stacking plot of x-ray diffraction patterns between 5 and 15 degree during compression. A broad peak centered at 9 degree is the liquid diffuse peak, the peak at 2θ = 13.5 degree is Cu (111) diffraction peak and the peak at 2θ = 14.7 degree is Kr-*fcc* (220) diffraction peak. The gray area illustrates the integrated area of liquid Kr. (B) The integrated area of liquid Kr (solid circles) on the left vertical axis and the pressure (open diamonds) on the right vertical axis as a function of time. The red lines are the exponential fits.

Fig. 4 The decay/growth time constants, τ (solid circles: compression, open circles (decompression) across the liquid-solid phase boundary as a function of compression rates in a linear scale and in a natural logarithmic scale (inset). The black line is the linear fit of the data during compression, and the red line is the linear fit of those during decompression.

Fig. 5 Three representative 2-D 2θ-time plots of time-resolved diffraction pattern (with a trapezoidal wave pressure modulation) at faster (a) ~8 GPa/s (50 ms exposure), moderate (b)

1.9(±0.1) GPa/s (200 ms exposure), and slower (c) 0.005(±0.001) GPa/s (500 ms exposure) compression rates with its measured pressure (solid circles) and the bars showing the calculated diffraction patterns of Cu (blacks), Kr-*fcc* (blues) and Kr-*hcp* (reds) at ~ 1.1 GPa.

Fig. 6 (A) Lattice parameter of Kr-*fcc* (symbols, left vertical axis) and pressure (open circles, right vertical axis) as a function of time. Different open symbols represent the lattice parameter calculated from different diffraction peaks and the average of lattice parameter shows in solid circles. (B) Lattice parameters of Kr-*hcp* (symbols, left vertical axis) and modulation waveform (black curves, right vertical axis) as a function of time. Different open symbols represent the lattice parameter calculated from different diffraction peaks and the averages of lattice parameters show in solid circles.

Fig. 7 (A) Volumes of Kr-*fcc* (solid symbols) and Kr-*hcp* (open symbols) at three representative dynamic loadings (1.9±0.1 GPa/s: circles, 0.07±0.03 GPa/s: triangles, and 0.02±0.009 GPa/s: diamonds) as a function of relative time, time/t_m (t_m: the modulation period). The inset plots the c/a ratios of Kr-*hcp* at all dynamic loadings as a function of time/t_m. The black line in the inset locates the ideal c/a ratio of *hcp*, 1.633. (B) Volumes of Kr-*fcc* (solid) and Kr-*hcp* (open) at dynamic loadings, volumes of *fcc* at static condition (curves), and volumes of *fcc* and *hcp* under laser-heating conditions (diamonds) as a function of pressure. The static P-V curve is calculated from the third-order Birch-Murnaghan equation[13]. The volumes of *fcc* and *hcp* is obtained from the previous laser-heating experiments [10]. The inset shows the representative hysteresis of *fcc* and *hcp* during compression (bottom) and decompression (top).

Fig. 8 The measured strain rate ($\Delta a/a_o/\Delta t$) of Kr-*fcc* as a function of compression rates. The solid circles are calculated under compression and the open circles are under decompression. The black line is the linear fit of the measured strain rates and compression rates.

Fig. 9 (A) The histogram of the time difference between when Kr-*fcc* first appears and when pressure starts to increase. (B) The histogram of the time difference between when Kr-*hcp* first appears and when pressure reaches the peak pressure. The red curves are the Gaussian fits and the inset of the bottom panel illustrates the threshold pressures when Kr-*hcp* appears.

References:

1. G. W. Lee, W. J. Evans, and C. S. Yoo, Phys. Rev. B 74, 134112 (2006).
2. G. W. Lee, W. J. Evans, and C. S. Yoo, Proc. Nat. Acad. Sci. U.S.A. 104, 9178 (2007).
3. J.-Y. Chen and C. S. Yoo, Proc. Nat. Acad. Sci. U.S.A. 108, 7685 (2011).
4. J.-Y. Chen and C. S. Yoo, J. Chem. Phys. 136, 114513 (2012).
5. D. Tomasino and C. S. Yoo, Appl. Phys. Lett. 103, 061905 (2013).
6. M. Ross and A. K. McMahan, in Physics of Solids Under High Pressure, edited by J. S. Schilling and R. N. Shelton (North-Holland, Amsterdam, 1981), p. 161.
7. A. K. McMahan, Phys. Rev. B 33, 5344 (1986).
8. A. P. Jephcoat, H. -k. Mao, L. W. Finger, D. E. Cox, R. J. Hemley, and C.-s. Zha, Phys. Rev. Lett. 59, 2670 (1987).
9. W. A. Caldwell, J. H. Nguyen, B. G. Pfrommer, F. Mauri, S. G. Louie, and R. Jeanloz, Science 277,9301 (1997).
10. H. Cynn, C. S. Yoo, B. Baer, V. Iota-Herbei, A. K. McMahan, M. Nicol, and S. Carlson, Phys. Rev. Lett. 86, 4552 (2001).
11. K. A. Goettel, J. H. Eggert, and I. F. Silvera, Phys. Rev. Lett. 62, 665 (1989).
12. R. Reichlin, K. E. Brister, A. K. McMahan, M. Ross, S. Martin, Y. K. Vohra, and A. L. Ruoff, Phys. Rev. Lett. 62, 669 (1989).
13. D. Errandonea, B. Schwager, R. Boehler, and M. Ross, Phys. Rev. B 65, 214110 (2002).
14. I. Kwon, L. A. Collins, and J. D. Kress, Phys. Rev. B 52, 15165 (1995).
15. R. Boehler, M. Ross, P. Söderlind, and D. B. Boercker, Phys. Rev. Lett. 86, 5731 (2001).
16. P. Tolédano, G. Krexner, M. Prem, H.-P. Weber, and V. P. Dmitriev, Phys. Rev. B 64, 144104 (2001).

17. D.A. Young, *Phase Diagrams of the Elements* (University of California Press, Berkeley, 1991).

18. R. Bruinsma and A. Zangwill, Phys. Rev. Lett. 55, 214 (1985).

19. W. J. Evans, C. S. Yoo, G. W. Lee, H. Cynn, M. J. Lipp, and K. Visbeck, Rev. Sci. Instrum. 78, 6 (2007).

20. Y. Wang, J. Zhang, H. Xu, Z. Lin, L. L. Daemen, Y. Zhao, and L. Wang, Appl. Phys. Lett. 94, 071904 (2009).

21. A.P. Hammersley, S.O. Svensson, M.Hanfland, A.N. Fitch, and D.Hausermann, High PressureRes.14, 235 (1996).

22. M. Avrami, J. Chem. Phys. 8, 212 (1940).

23. J. J. Jonas, X. Quelennec, L. Jiang and T. Martin, Acta Mater. 57, 2748 (2009).

24. M. G. Evans and M. Polanyi, Trans. Faraday Soc. 31, 875 (1935).

25. A. Polian, J. M. Besson, M. Grimsditch, and W. A. Grosshans, Phys. Rev. B 39, 1332 (1989).

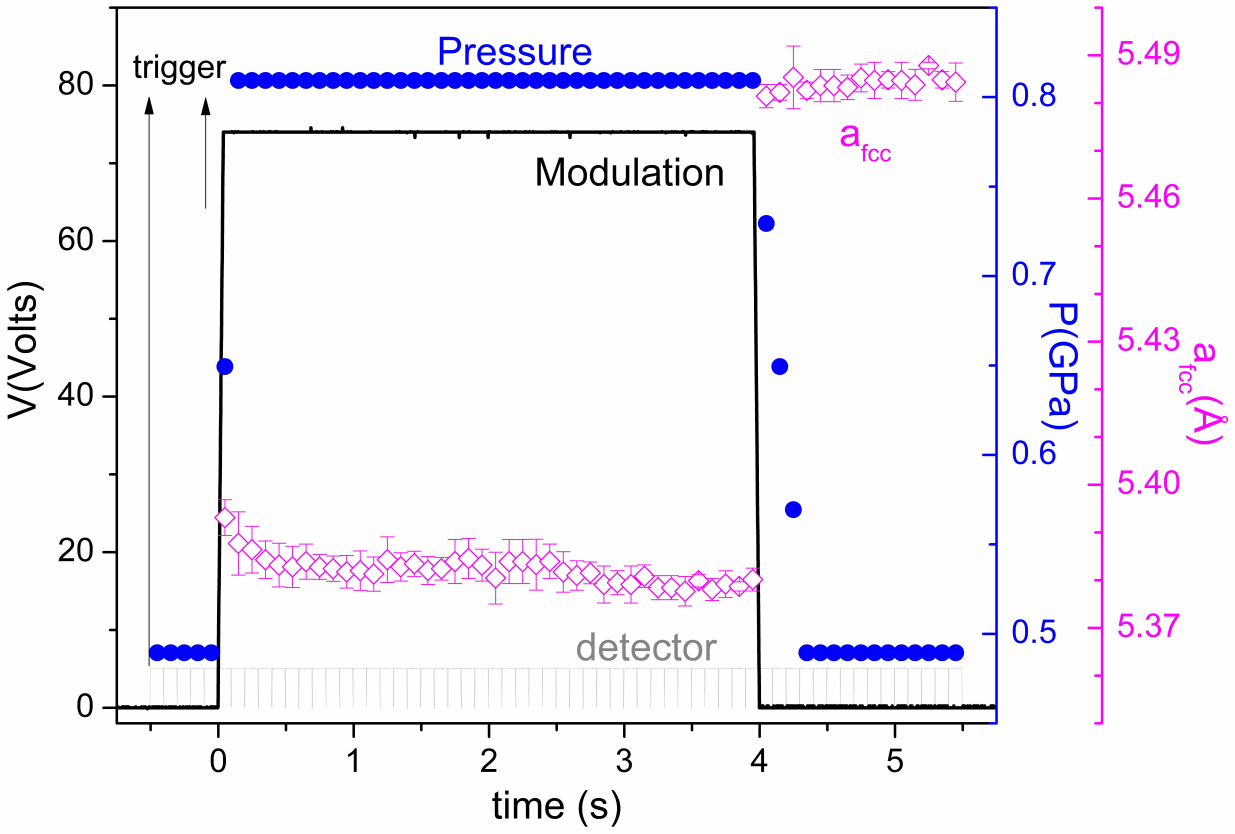

Figure 1 BP12060 22SEP2014

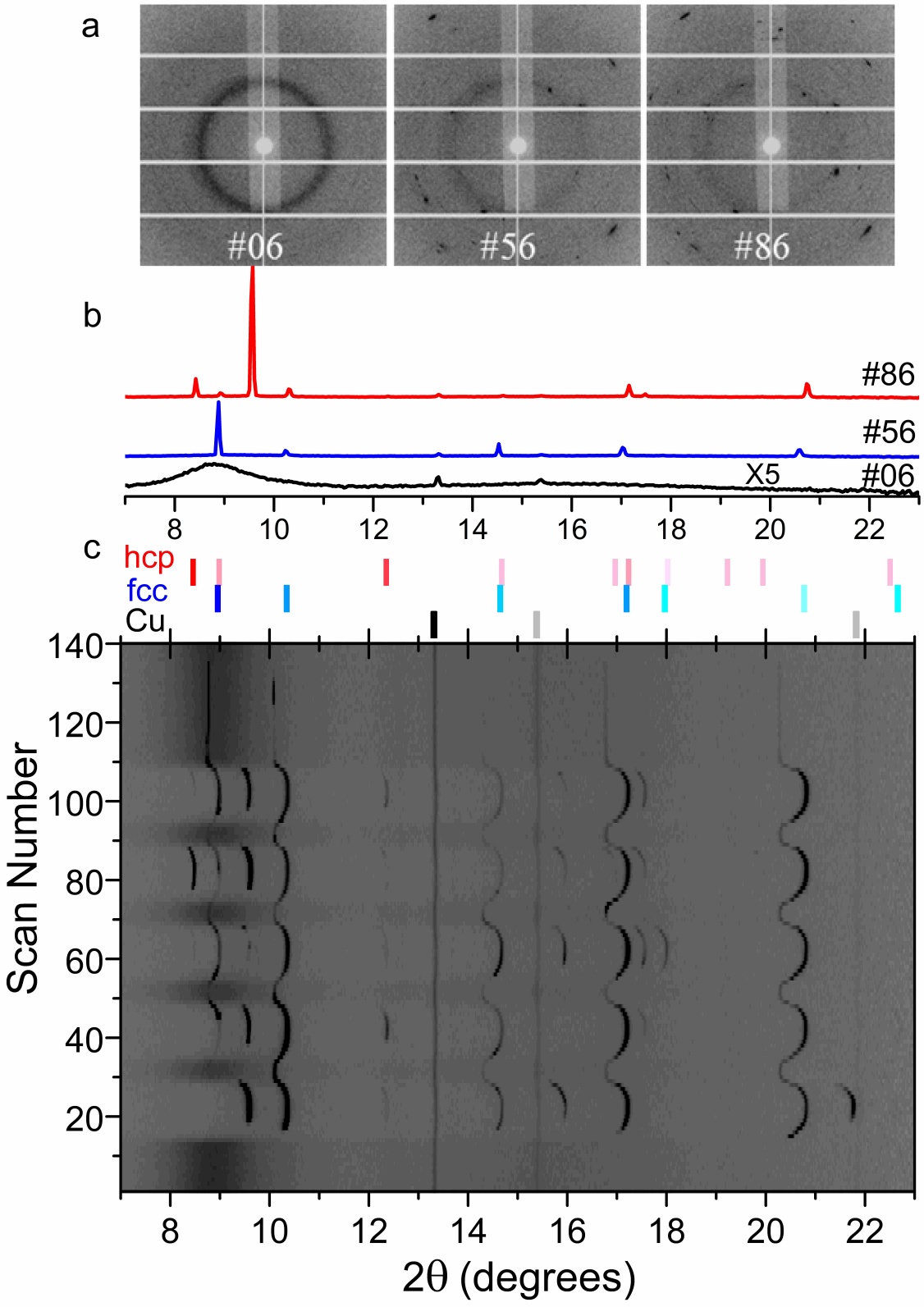

Figure 2 BP12060 22SEP2014

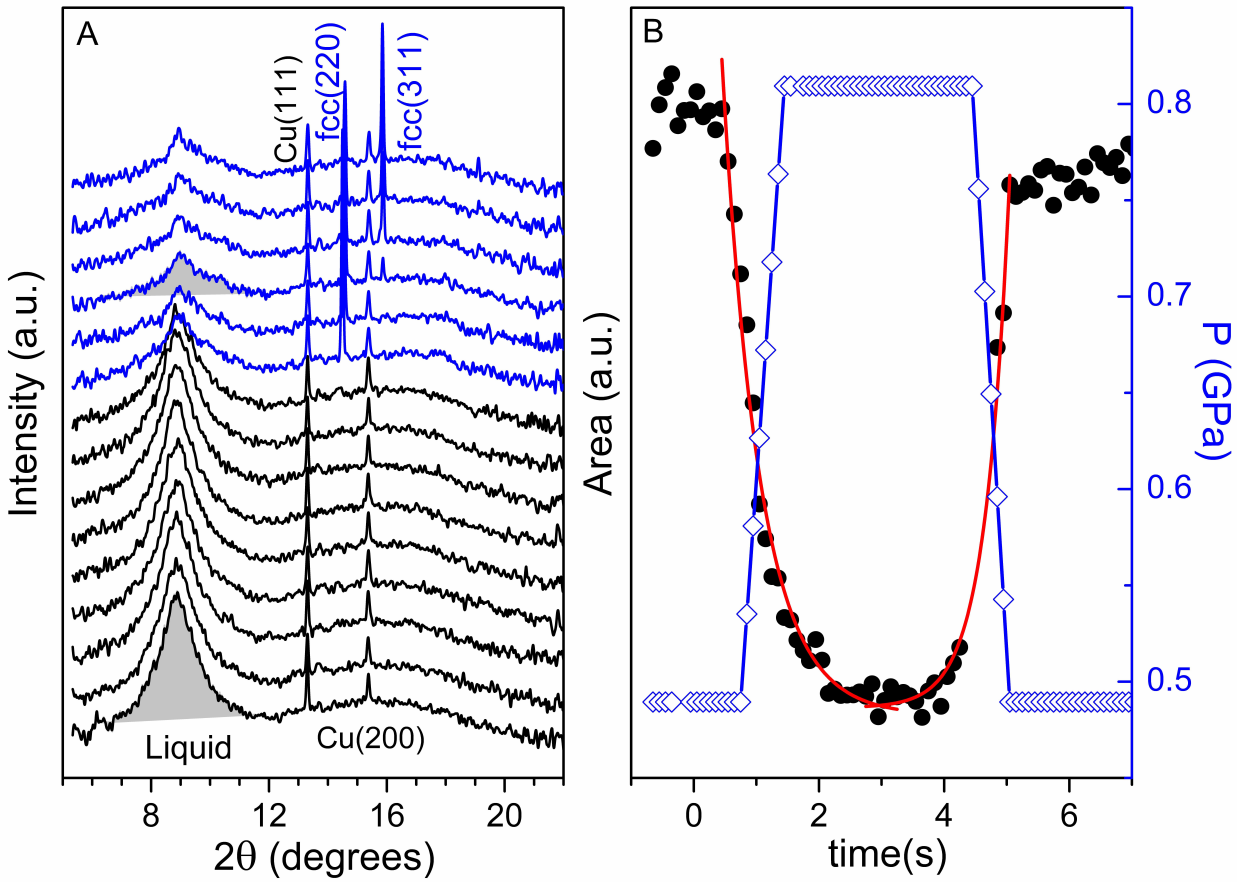

Figure 3 BP12060 22SEP2014

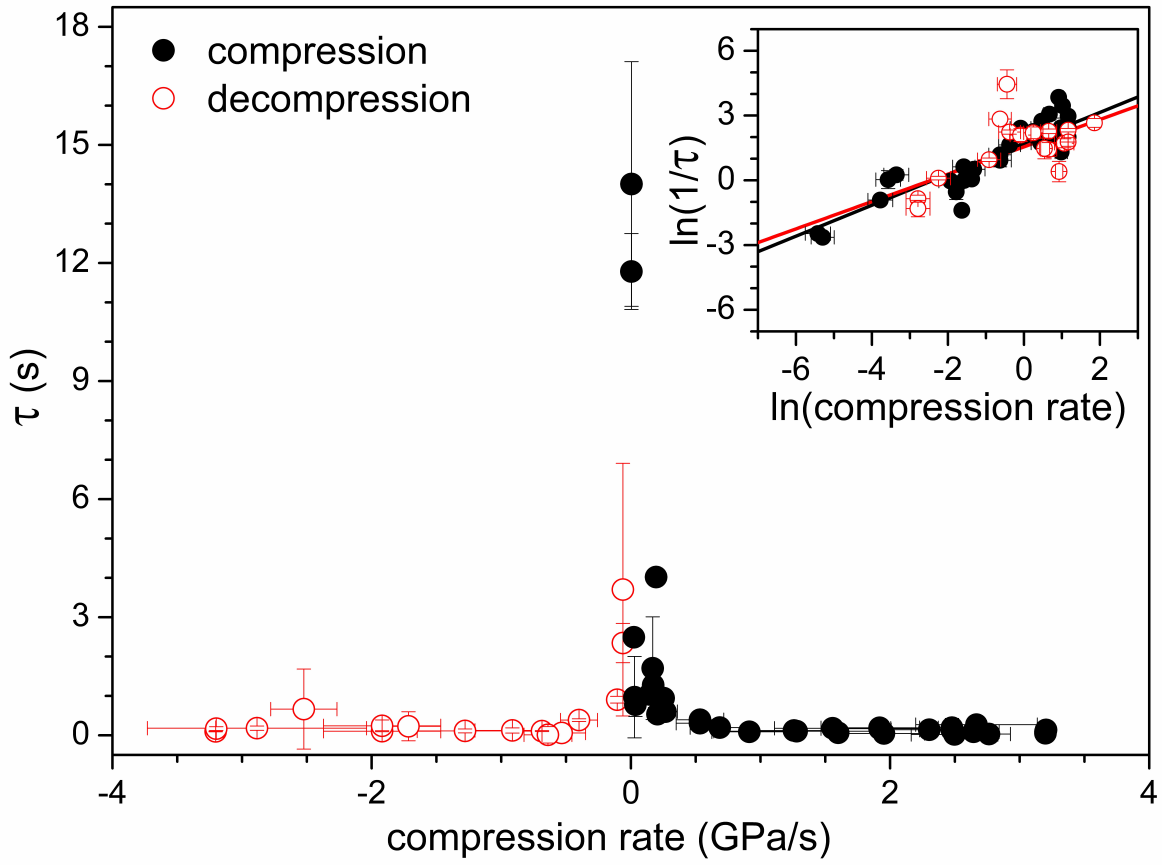

Figure 4 BP12060 22SEP2014

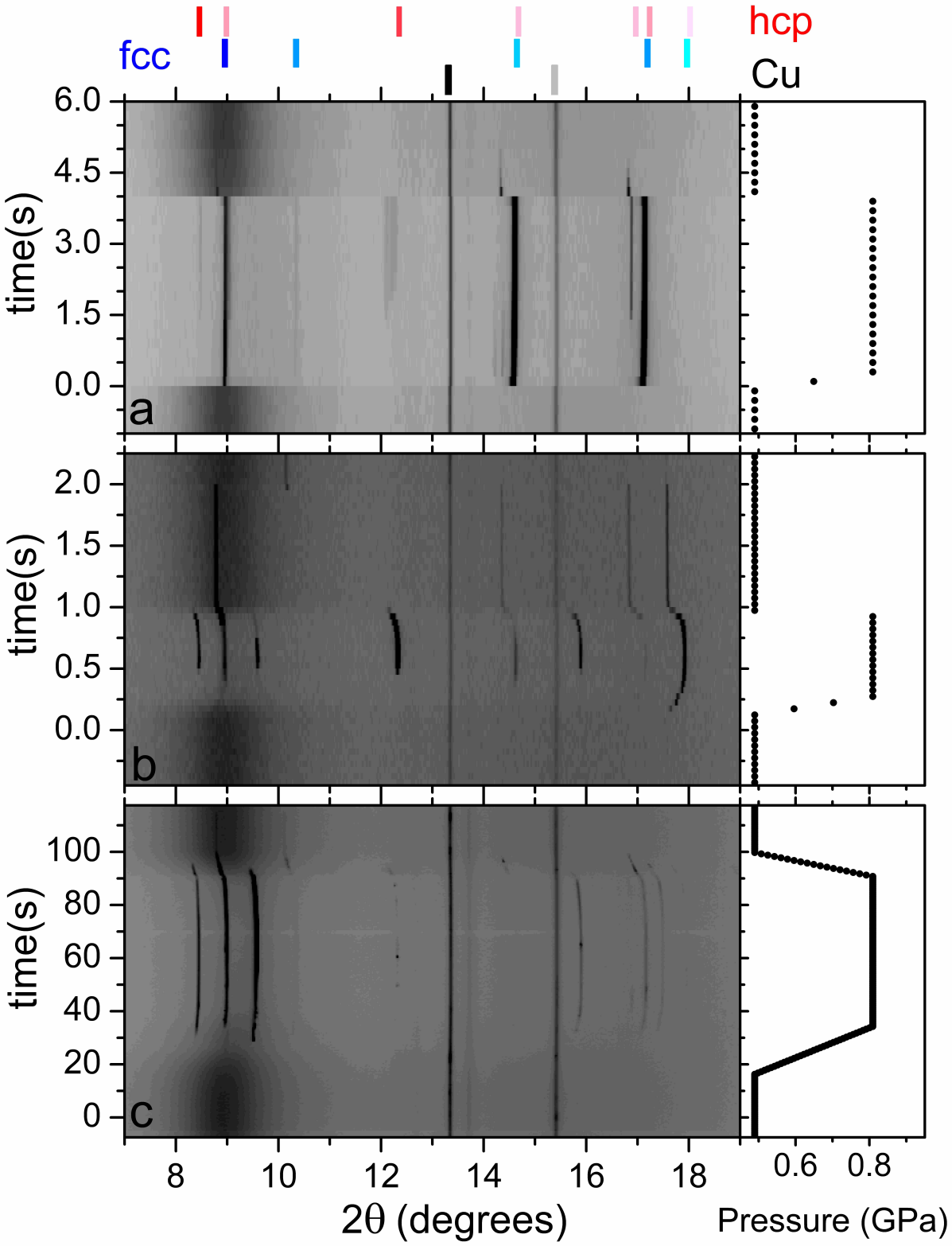

Figure 5 BP12060 22SEP2014

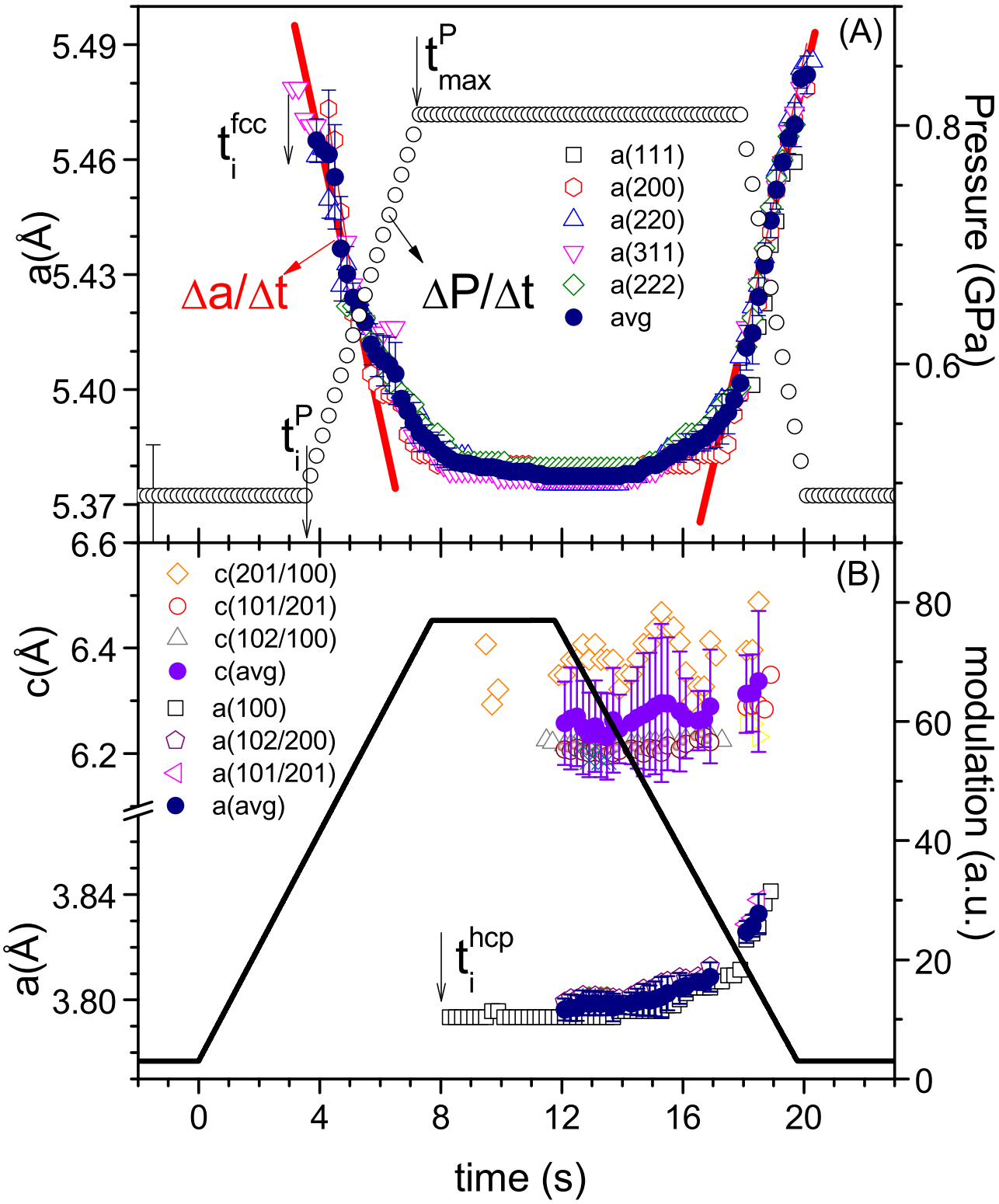

Figure 6 BP12060 22SEP2014

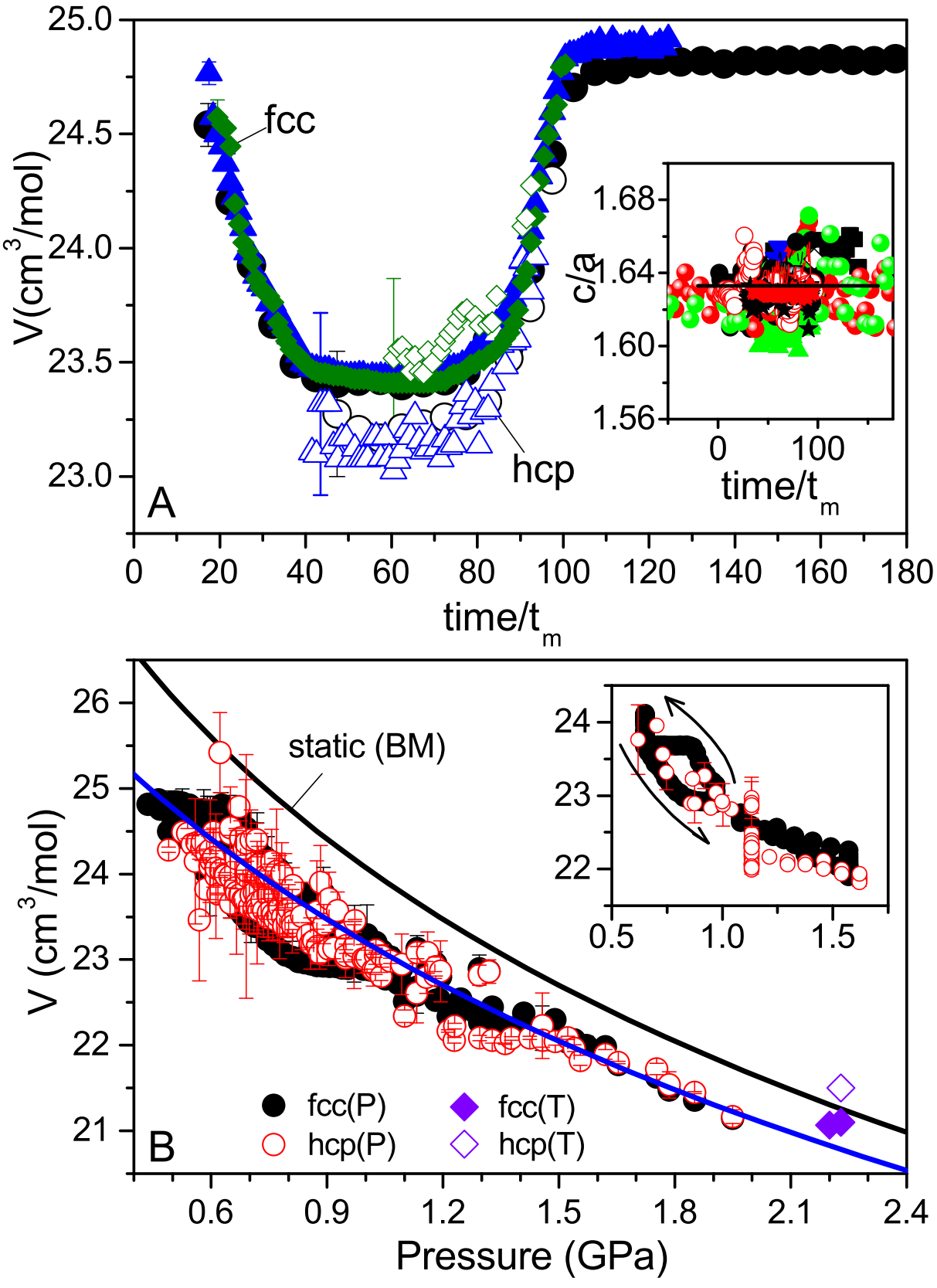

Figure 7 BP12060 22SEP2014

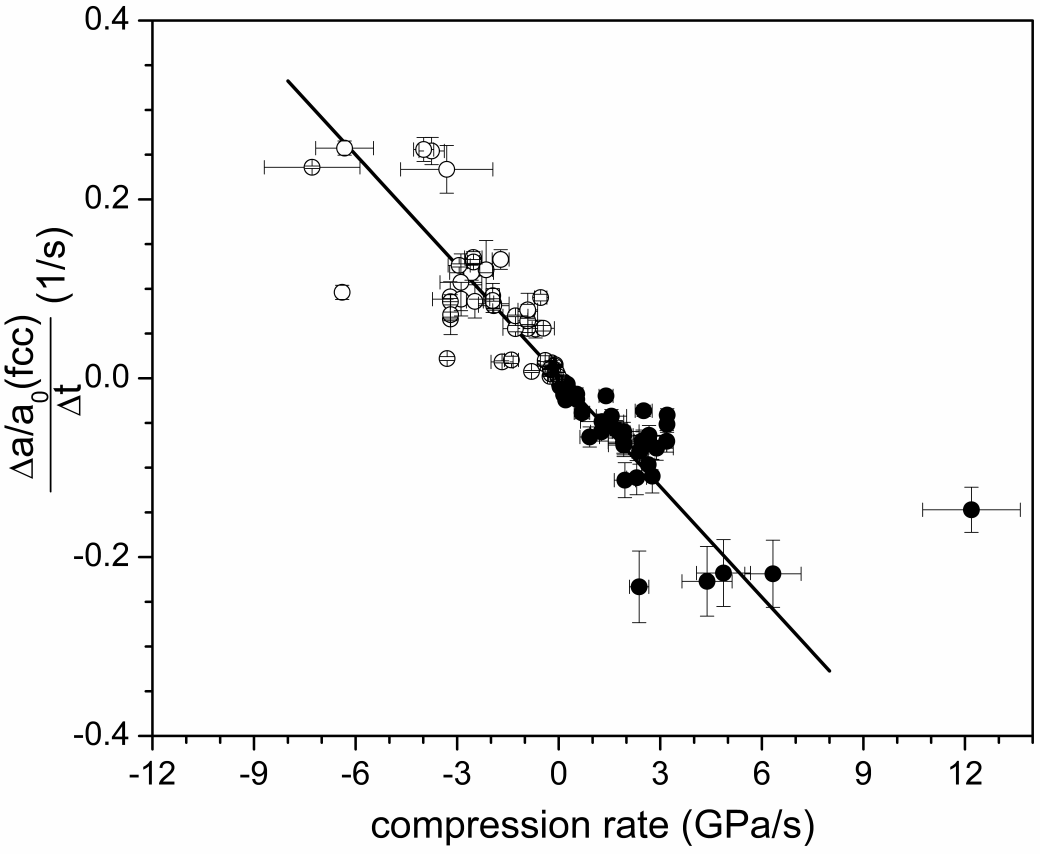

Figure 8 BP12060 22SEP2014

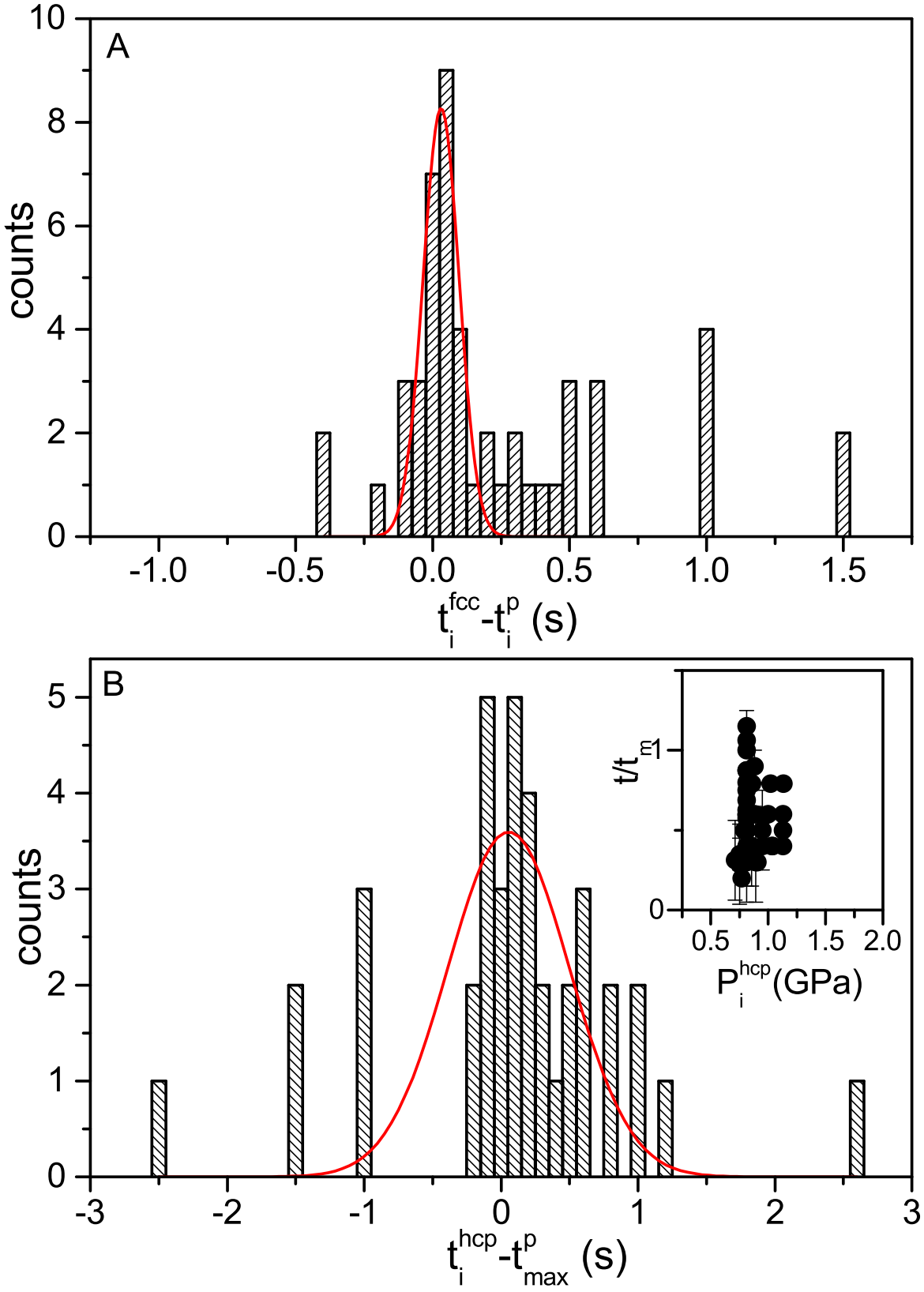

Figure 9 BP12060 22SEP2014